Chapter 3

Simulation of mixing of heterogeneous HE components

The majority on high explosives (HEs) used are blend ones. Properties of components differ that produces interaction on the grain scale (mesoprocesses). Lattice methods are suitable to investigate the hydrodynamic interaction of components.

Mixing of fluids due to their hydrodynamic interaction was so far mainly investigated for sparse systems. Mainly, a flow of one gas or liquid around a bubble or a drop of another gas or liquid was studied [87–90]. Several experiments dealt with a few inclusions, including ones of different size [91,92]. Comparison of theoretical, experimental and computation results was performed in [93].

The typical example of blend HE is the TNT/RDX composition. Here, the concentration of both components is not small (compositions such as TNT/RDX 50/50 are of practical interest). Account of mixing of HE components is particularly important to understand the process of detonation synthesis of diamond.

At high concentration, it is natural to consider a constrained flow, with periodic boundary conditions. From the computation viewpoint, this statement of the problem is even simpler, because the boundary conditions for a single inclusion are nontrivial. As a first approximation, one can consider the flow of one gas around a region of another gas with close density.

Computation of instability development and mixing is rather complicated for traditional finite-difference methods. At the same time, such problems are naturally formulated in the lattice methods, moreover, the unknown boundaries between regions occupied by different substances are obtained automatically. Lattice gas simulations of the Kelvin–Helmholtz instability was performed in [94], of the Rayleigh–Taylor instability — in [94,95]. The LBE method was also used to simulate the Rayleigh–Taylor instability in [72] and to simulate drop

deformation in shear flow in [96].

Experimental indications to the presence of component interaction in detonation products (DP) were obtained at the investigation of electric conductivity. Conductivity of DP of TNT/RDX mixture decreases monotonically with the increase in RDX fraction. Recent experiments showed that conductivity depends not only on the RDX fraction but also on the size of RDX particles [97]. Conductivity of coarse-grained compositions is higher, in some cases by an order of magnitude. Characteristic time of conductivity decrease also grows with increase in particle size. One of the causes of this effect can be mixing of DP of TNT and RDX behind the detonation front [9]. Conductivity of DP of TNT and RDX differ significantly (conductivity of TNT is high due to the release of free carbon), therefore, electric current flows mainly through the connected region consisting of DP of TNT. Amount of pure DP of TNT decreases due to diffusion mixing; hydrodynamic interaction can twist, elongate and break connected conductive region. Both effects should lead to the decrease in conductivity.

The diffusive mixing is effective for small particles only (thickness of the diffusive layer is of order of 2 mkm for 1 mks) [98]. For large particles, one should consider the effect of hydrodynamics and compute emerging flows. Relative velocities u of order of hundreds meters per second can arise in DP due to difference in properties of individual HEs (V.V. Mitrofanov, V.M. Titov [98]). The tangential velocity discontinuity exists at the grain boundaries, and the Kelvin–Helmholtz instabilities develop.

3.1 Diffusion

The effect of molecular diffusion was investigated by the LGA method in two geometries. The model with 9 velocity vectors was used [20] (fig. 1.3). The diffusivity $D = 0.56$ (in lattice units) was determined by the comparison of the numeric and the analytic self-similar solutions for the contact of two half-spaces of different color.

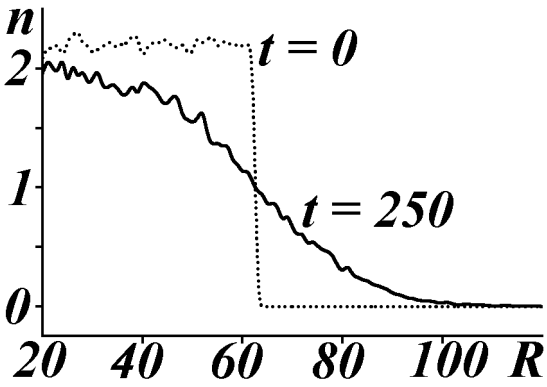

Figure 3.1.

The evolution of the round region of one gas surrounded by another gas is shown in fig. 3.1. Radial dependence of concentration is given for two time instants. If we suppose the drop diameter (125 lattice units) to be 5 mkm, and the diffusivity to be $D = 0.04$ cm^2/s, then 250 time steps correspond to 0.056 mks. Here, the

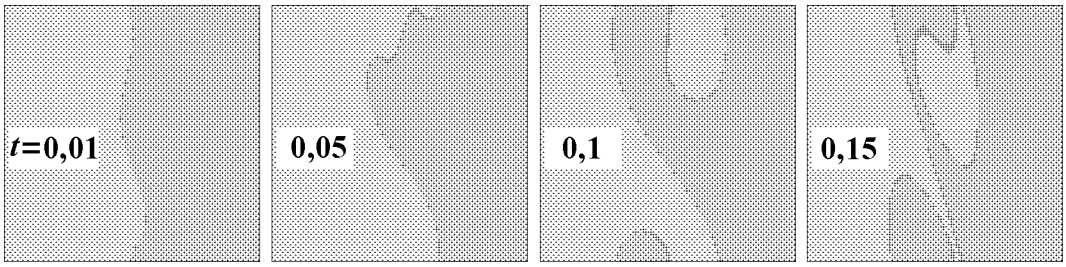

Figure 3.2. Instability of the tangential discontinuity.

diffusion is already significant.

The LGA model is able to take into account diffusion as a physical process, which is a certain advantage. The computation experience showed however that the transition to larger particles and inclusion of hydrodynamic interactions required the unreal increase in the computation scale. The Kelvin–Helmholtz instability was therefore computed by the LBE method which is more flexible. The LBE model on the square grid with 9 possible velocity vectors was used (fig. 1.4,*a*).

3.2 Small-scale instabilities

Figure 3.2 presents an example of such instability (time is in microseconds).

On different sides of the interface, the initial velocity had opposite directions. The interface was given by the equation $x = L/2+3(\cos(2\pi y/L)+\cos(3\pi y/L))$, here $L = 100$ is the size of computation cell. On the top and bottom boundaries, periodic boundary conditions were imposed, and the right and left boundaries were rigid walls without friction. The Reynolds number calculated by the size of the cell was $\mathrm{Re} = 2uL/\nu \approx 500$. The growth of initial perturbations proceeded, then the turnover of wave crests and the formation of vortices. A black layer at the interface is a region were the diffusive mixing is substantial. The recalculation to the physical values gives the size of the cell of about 10 mkm (assuming $\nu = 0.04$ cm^2/s [99], and $u = 200$ m/s). Therefore, these results can be treated as a small-scale "secondary" instability on the drop surface.

3.3 Flow around the cylinder

Figure 3.3 shows the development of the flow of fluid 1 (light region, moves to the right) around the initially round drop of fluid 2 (dark region, moves to the left). In this and following computations of this chapter, both the horizontal and vertical boundary conditions were periodic. The Reynolds number calculated by the drop diameter was about 1530 for fig. 3.3,*a* (size of computation cell

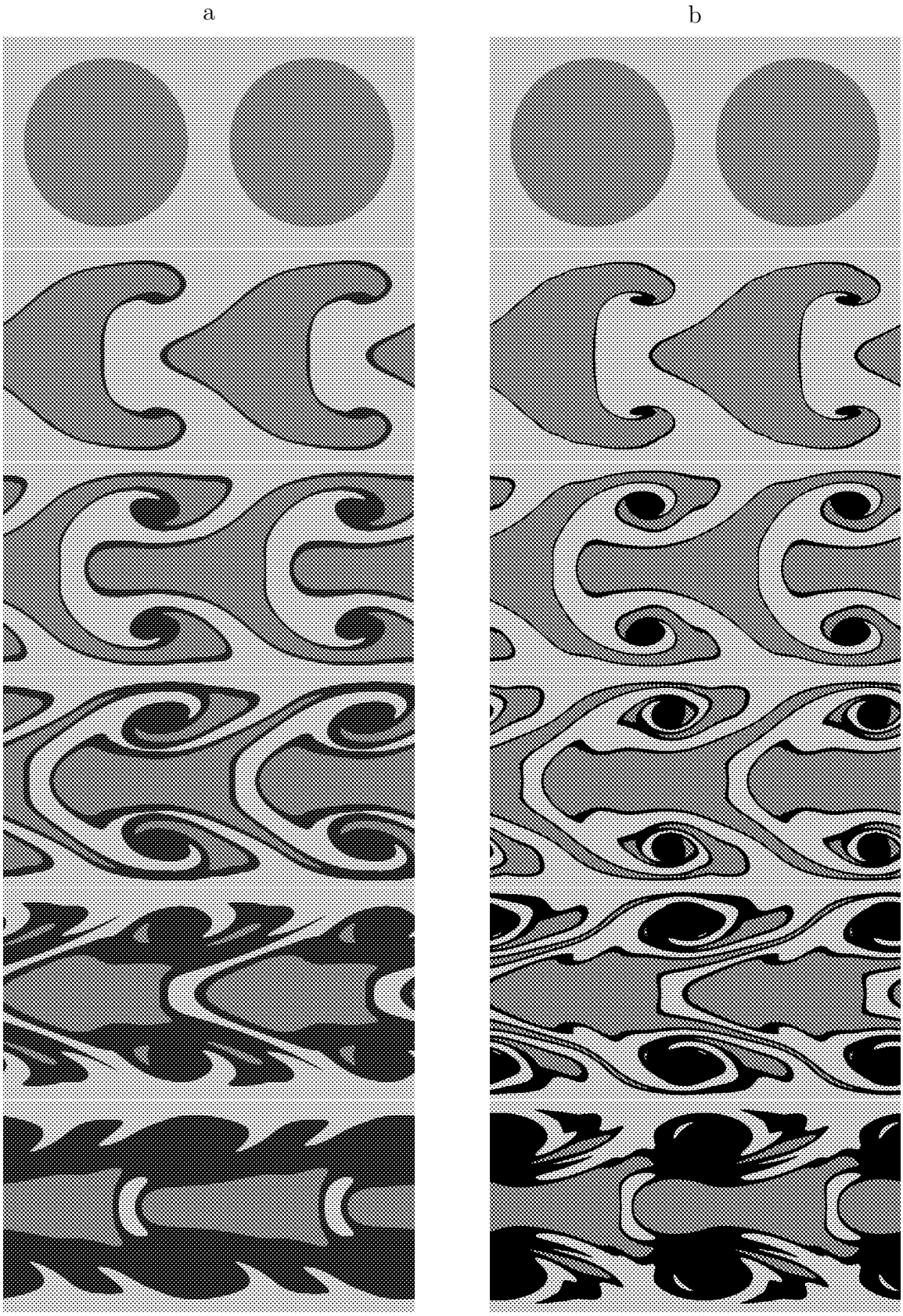

Figure 3.3. Instability development and mixing at the flow around cylinder. Reynolds number $\mathrm{Re} \approx 1530$ (*a*), and $\mathrm{Re} \approx 4900$ (*b*). Time (from top to bottom) $t/t_f = 0$, $t/t_f = 1$, $t/t_f = 2$, $t/t_f = 3$, $t/t_f = 4$, $t/t_f = 5$

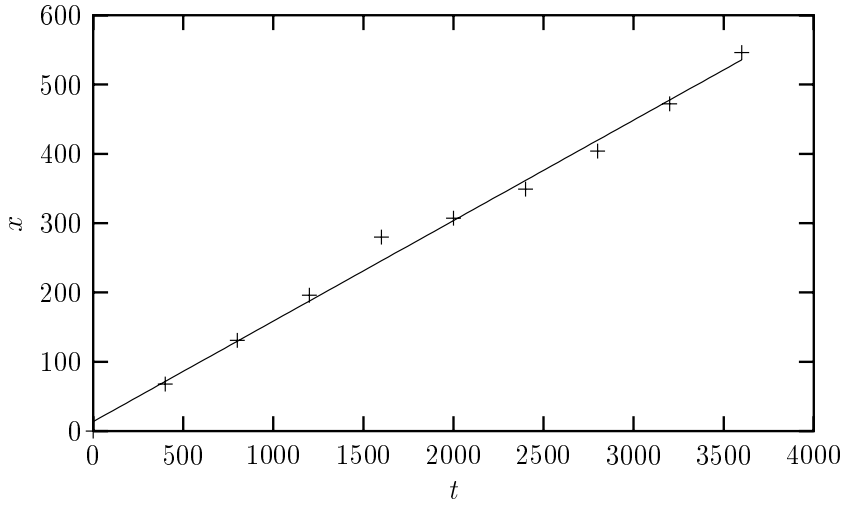

Figure 3.4. Time dependence of the "drop" front point

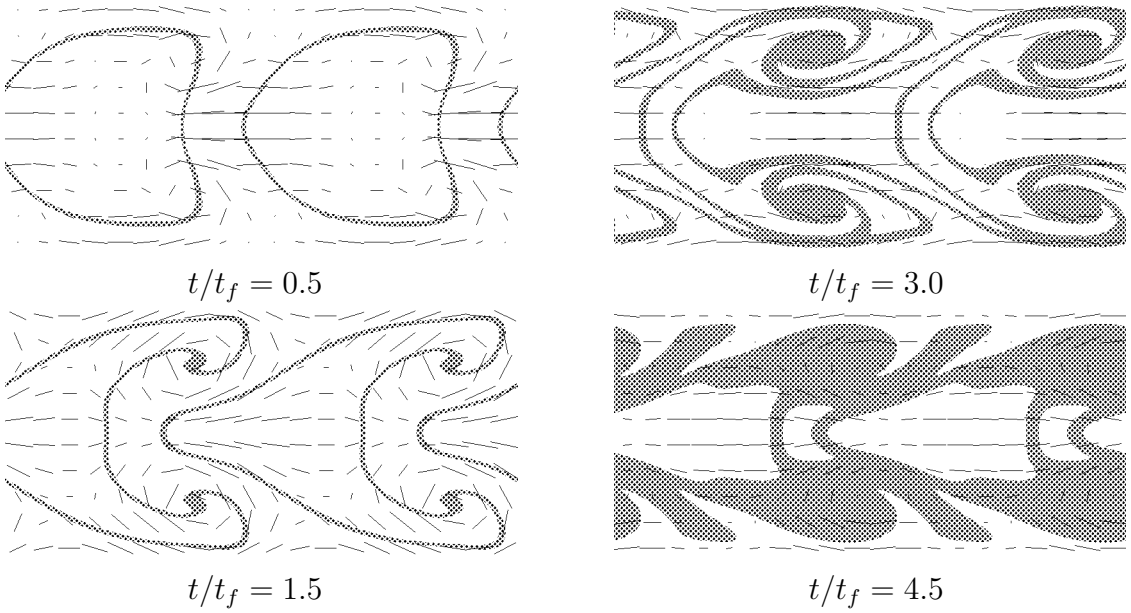

Figure 3.5. Velocity field in the flow around the cylinder. The flow corresponds to the fig. 3.3. The region of diffusive mixing is grayed

was $L = 400$, velocity of drop and surrounding flow was $u = \pm 0.2$, kinematic viscosity was $\nu = 1/12$, drop diameter was $d = L\sqrt{\frac{2}{\pi}}$ — drop occupied half of cell volume) and $\mathrm{Re} \approx 4900$ for fig. 3.3,b (here, the the size of computation cell was doubled, $\nu \approx 0.05$). The characteristic flow time was $t_f = d/2u$. If we suppose $u = 100$ m/s, then $t_f \approx 5d$ mks (d in millimeters).

At the instability development, the boundary elongated and twisted and vortices arose. The region is shown with black, where the absolute value of concentration difference of components $|\rho_1 - \rho_2|$ is less than $0.3\rho_0$. In this zone, a diffusive mixing can be regarded substantial.

It is of interest to consider the motion of the front poind of "drop". Figure

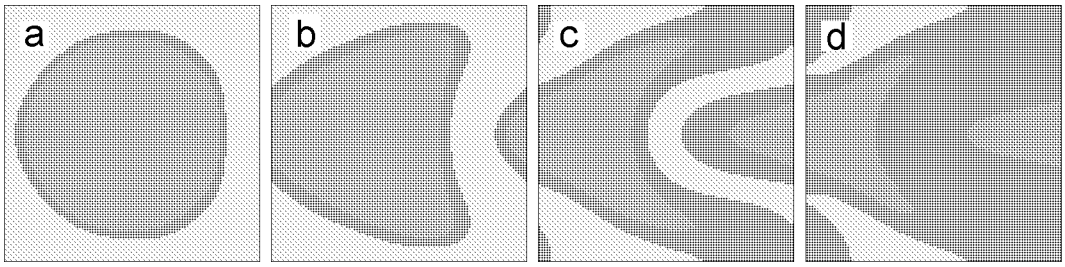

Figure 3.6. Instability development leading to the break of current channels. Dimensionless time $t/t_f = 0.25$ (a), 0.75 (b), 2.0 (c) and 2.75 (d)

3.4 indicates that its velocity remains virtually constant despite the resistance of counter-flow. The average velocity of the drop "nose" calculated by the least-square method was $v \approx 0.145 \pm 0.004$ (strait line in fig. 3.4). This effect is caused with a formation of the flow in the form of a vortex ring (fig. 3.5). Since vortex rings can maintain their individuality for a long time, their formation should lead to the slowing down of the mixing at its later stages.

In the case of smaller particles, the overlapping of tongues of mixed substance is possible (fig. 3.6, here $Re \approx 200$). Clearly, it should lead to sharp decrease in the electric conductivity due to disappearance of the connected net of conducting channels.

3.4 Effect of the initial system geometry

In the real TNT/RDX "alloy", RDX particles are not round. Rather, grains are polyhedral. Therefore, the influence of peculiarities of the shape of initial inclusionx on the hydrodynamic interaction of components is of interest. Figure 3.7 presents different stages of instability development in the flow around initially square "drops" with different initial orientation relatively to the flow. The process is in general similar to the fig. 3.3, but the mixing is faster due to the presence of corners, at which instabilities develop faster.

In all computations above, drops were initially placed at nodes of a simple square lattice. It is of interest to investigate the change of mixing pattern for the initial layout with different symmetry.

In the next series of computations, the initial drop layout was diagonal (the square lattice, rotated by 45° over the relative velocity vector — the "checkerboard" layout). That is, the coordinates of a center of one round drop were (0,0) (this drop appears as four regions in the corners of the computation cell because of periodic boundary conditions). Another drop was placed in the center of cell. The computations were also carried out, with one drop sub-system shifted rel-

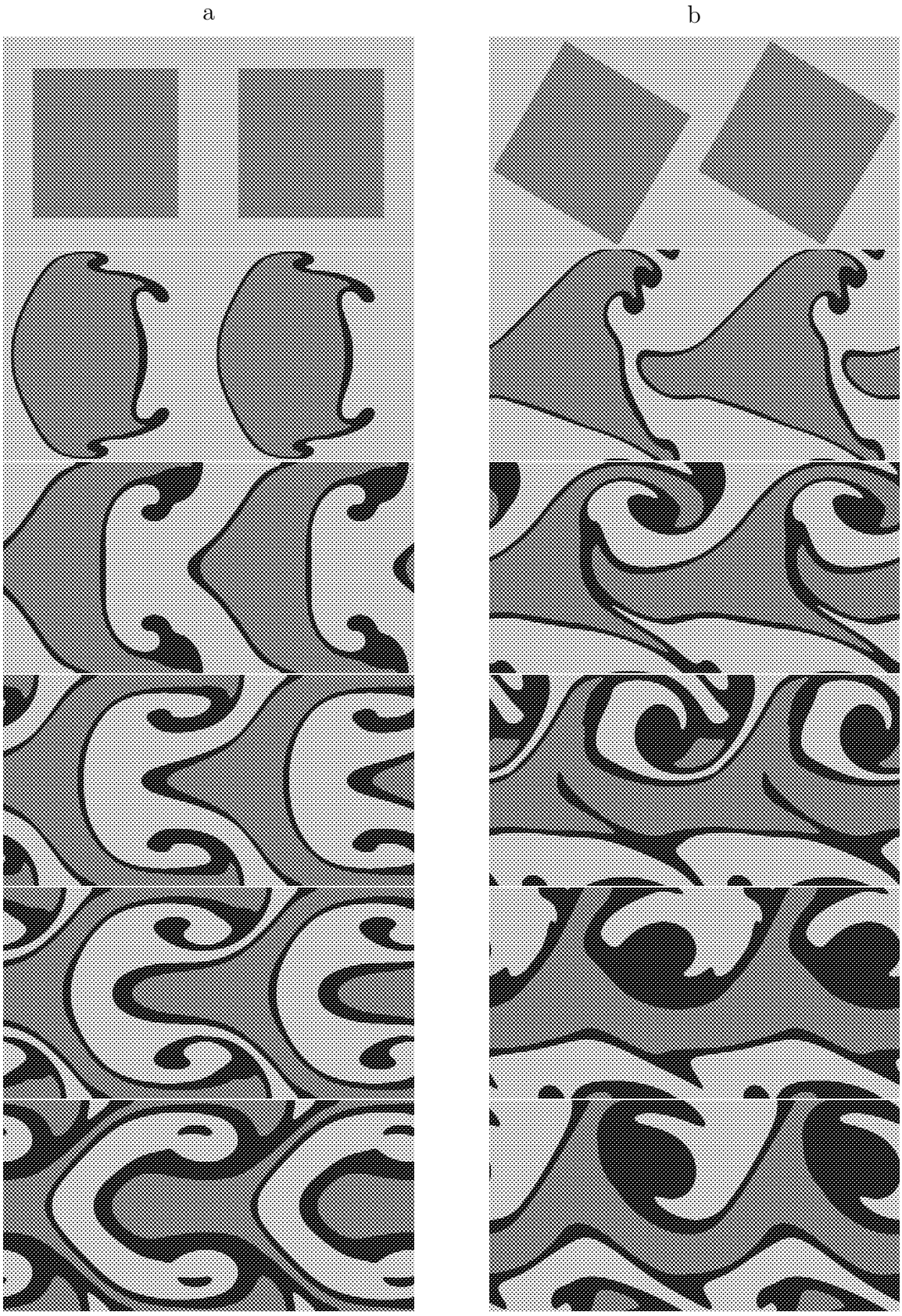

Figure 3.7. Instability development and mixing at the flow around square. Reynolds number is Re ≈ 800. Time (from top to bottom) $t/t_f = 0$, $t/t_f = 1$, $t/t_f = 2$, $t/t_f = 3$, $t/t_f = 4$, $t/t_f = 5$. Square was initially perpendicular to the flow (a) and rotated by 30° (b)

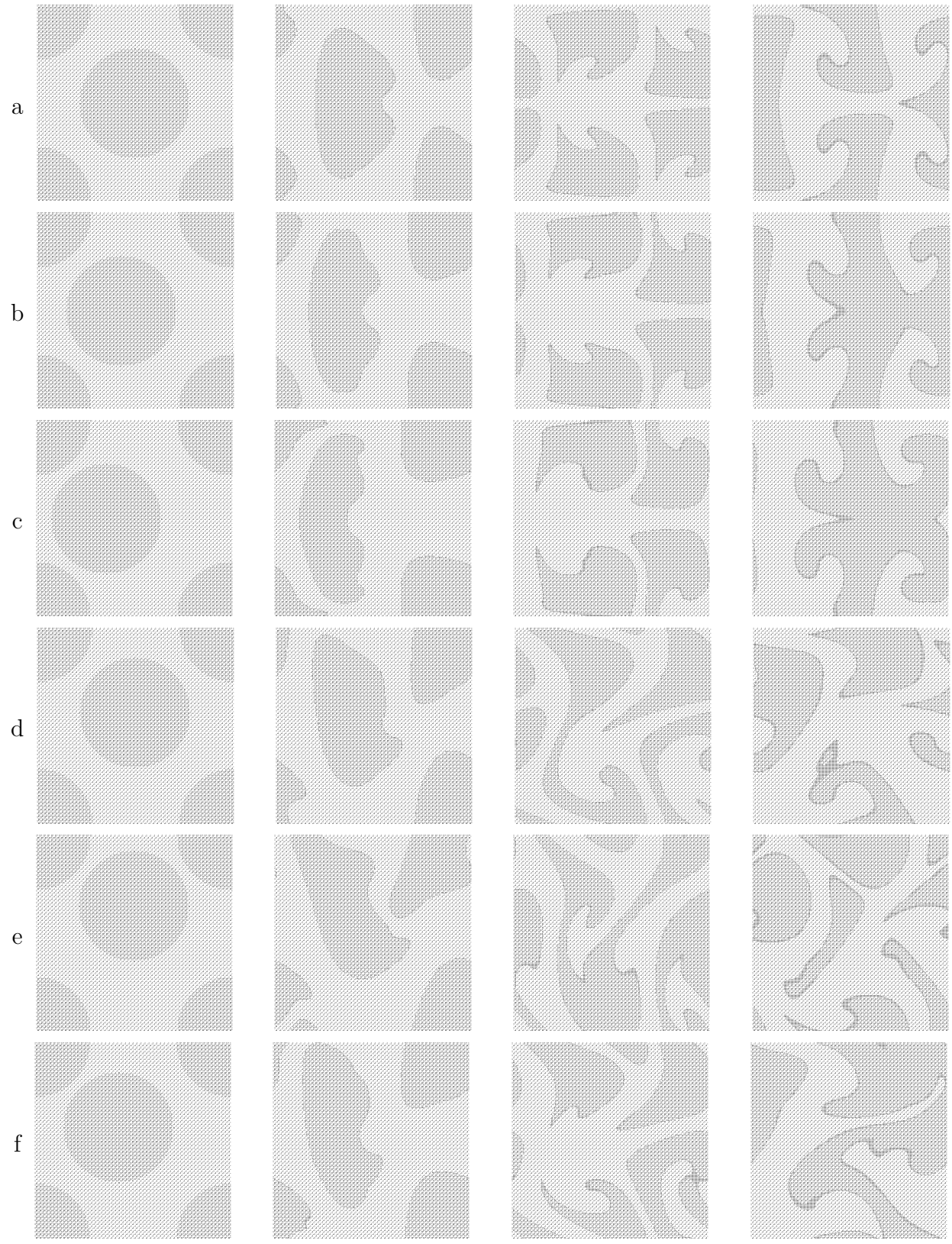

Figure 3.8. Flow for the "diagonal" drop layout. Displacement of the central cylinder is *a*: $(\Delta x, \Delta y) = (0, 0)$, *b*: $(\Delta x, \Delta y) = (-d/8, 0)$, *c*: $(\Delta x, \Delta y) = (-d/4, 0)$, *d*: $(\Delta x, \Delta y) = (0, d/8)$, *e*: $(\Delta x, \Delta y) = (0, d/4)$, *f*: $(\Delta x, \Delta y) = (-d/8, d/8)$

ative to another one in horizontal or vertical direction (this was attained by the shift of the central drop). In all computations, the size of computation cell was $L = 200$, the flow velocity was $u = 0.2$, the kinematic viscosity was $\nu = 1/12$, the drop diameter was $d = L/\sqrt{\pi} \approx 112$, the characteristic flow time was $t_f \approx 280$, and the Reynolds number was $\mathrm{Re} \approx 540$). Development of instabilities for different initial layouts is presented in fig. 3.8. For all series, the first frame corresponds to $t/t_f = 0$, the second one to $t/t_f = 1$, the third one to $t/t_f = 3$, and the fourth one to $t/t_f = 5$.

The flow pattern for the "checkerboard" initial layout of inclusions differs appreciably from the case of the simple lattice. The flow changed rapidly from the mainly horizontal one to the mainly vertical flow with a system of vortices. A substantial deformation of drops occured, with their fragmentation and merging of fragments at later stages. In some cases, a blocking of the cell with on of the direction happened (e.g., fig. 3.8,b,c,e,f).

3.5 Mixing due to the pulse acceleration

The velocity discontinuity may arise as a result of the passage of shock waves through the interface of fluids with different density (Richtmyer–Meshkov instability, RM) or the acceleration of the medium which is analogous to the action of gravitation (Rayleigh–Taylor instability, RT). RT instability corresponds to the constant acceleration, for the RM instability, time dependence of acceleration is given by δ-function.

In this work, an intermediate case was considered — horizontal acceleration was $a = a_0$ at the time interval $0 \le t \le t_f$, later, acceleration turned zero. Characteristic flow time was $t_f = d/2u$, the value of acceleration was chosen so as $a_0 = u/t_f$. Size of computation cell was $L = 400$, velocity $u = 0.2$, cylinder initially occupied half of the cell.

The action of forces on the substance was calculated in the Boussinesq approximation: the force acting on the substance at a node $\mathbf{x}$ is $\mathbf{F}(\mathbf{x}) = \mathbf{a}(\rho_1(\mathbf{x}) - \rho_2(\mathbf{x}))$. Development of instability is presented in fig. 3.9. Density distribution during the mixing process is similar to the case presented in fig. 3.3. This fact justifies the simplified formulation used in sections 3.2–3.4.

3.6 Computation of the electric conductivity

The electrical conductivity of the cell was computed based on the hydrodynamic configurations obtained using the relaxation method. The electric potential

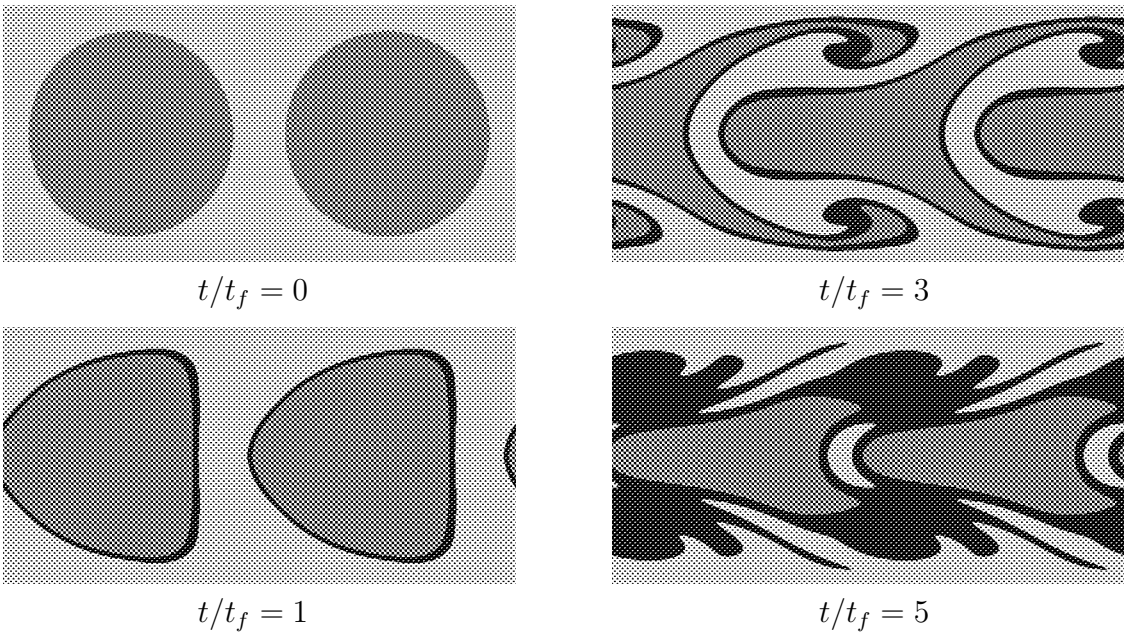

Figure 3.9. Mixing due to the Raylegh–Taylor instability

was specified at the opposite edges of the cell ($\varphi = 0$ at one edge, $\varphi = \varphi_0$ at the opposite one) and the conductivity of each lattice link was calculated as $Y_{ij} = \sigma_0 h \sqrt{n_i n_j}$. Here, σ_0 is a constant, n_i, n_j are the "effective concentrations" of the conductive phase at terminal nodes of a link ($n = \max(\rho_{TNT} - \rho_{RDX}, 0)$), h is the lattice spacing. This formula reflects both the "dilution" of highly conductive DP of TNT and the "poisoning" of the conductivity at the mixing (which can result from secondary chemical reactions between DP of TNT and RDX leading, e.g., to the burning of free carbon). Then, the equations of conductive charge transfer

$$\partial q/\partial t = -\mathrm{div}\ \mathbf{j} = -\mathrm{div}(\sigma \mathbf{E})$$

were solved along with the Poisson's equation for the electric potential $\Delta\varphi = -4\pi q$ using the time-implicit scheme of [100]. The changes of node charges Δq_i were calculated using the potential values obtained. Calculations continued until the maximum change $|\Delta q_i|$ became lower than a specified value. Then, the current through the cell was calculated as $I = \sum\limits_i Y_{i0} \Delta\varphi_i$, where the summation was over a layer adjacent to one of the edges with fixed potential. The cell conductivity $Y_x = I_x/\varphi_0$ was computed in the horizontal direction, $Y_y = I_y/\varphi_0$ — in the vertical one. In following graphs, the averaged value $\langle Y \rangle = (Y_x + Y_y)/2$ is shown.

Several computations of time dependence of the electric conductivity were performed for different drop diameters d. The results are presented in fig. 3.10. The time of the conductivity decrease increases with the enlargement of the

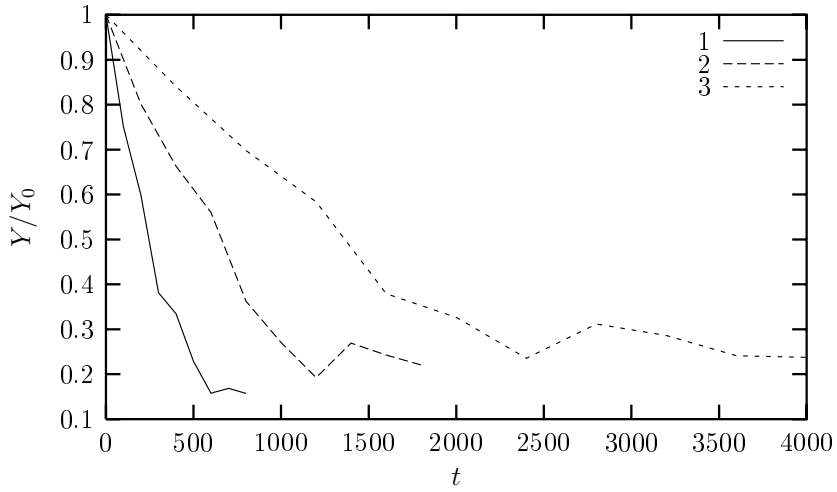

Figure 3.10. Time dependence of the electric conductivity. 1 — $d = 80$, 2 — $d = 160$, 3 — $d = 320$

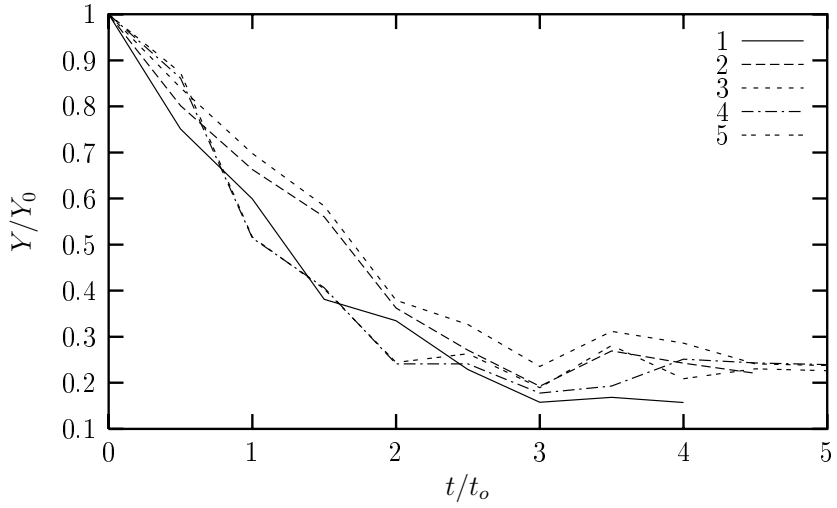

Figure 3.11. The dependence of the electric conductivity on the dimensionless time t/t_f. 1 — $Re \approx 400$, 2 — $Re \approx 800$, 3 — $Re \approx 1600$, 4 — $Re \approx 2550$, 5 — $Re \approx 4900$

drop size, therefore the average value of conductivity is greater for the coarse-grain medium, in agreement with experimental results of [97].

The dependence of conductivity on the dimensionless time t/t_f for different Reynolds numbers is also presented in fig. 3.11. Graphs virtually coincide, thus, the mixing is virtually self-similar.

Figure 3.12 presents time dependencies of the conductivity for inclusions of different shape. The cell conductivity decreases faster for square inclusions than for round ones, although graphs are qualitatively close.

Figure 3.13 presents the time dependence of the cell conductivity for the diagonal initial drop layout (curve 1, corresponds to fig. 3.8,*a*), for the horizontal shift of one sub-system of cylinders by $\Delta x = -d/4$ (curve 2, corresponds to fig. 3.8,*c*), for the vertical shift by $\Delta y = d/4$ (curve 3, corresponds to fig. 3.8,*e*),

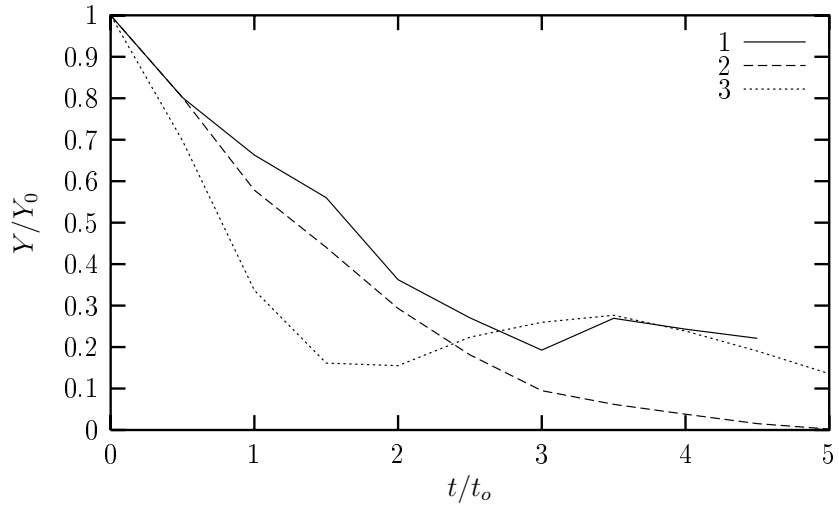

Figure 3.12. The dependence of the electric conductivity on the dimensionless time t/t_f for different drop shape. 1 — cylinder (fig. 3.3,), 2 — square (fig. 3.7,*a*), 3 — slanted square (fig. 3.7,*b*). In all cases $Re \approx 800$

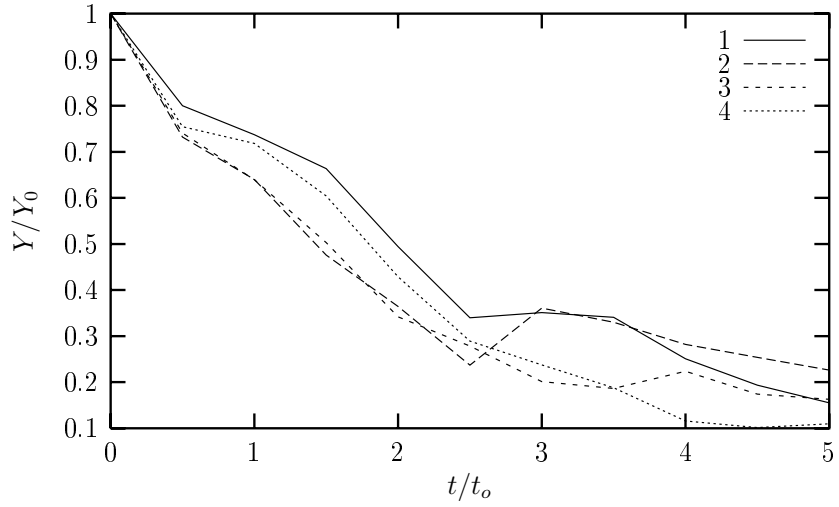

Figure 3.13. The dependence of the electric conductivity on the dimensionless time t/t_f for diagonal drop layout. 1 — see fig. 3.8,*a*, 2 — see fig. 3.8,*c*, 3 — see fig. 3.8,*e*, 4 — see fig. 3.8,*f*

and for both the horizontal and vertical shift by $\Delta x = -d/8, \Delta y = d/8$ (curve 4, corresponds to fig. 3.8,*f*). Conductivity decrease for "shifted" layouts is faster, although graphs are close.

Characteristic time of conductivity decrease by e times was $\tau \approx 2t_f$ in all cases. For drops of 200 mkm it gives 2 mks, with quite good agreement with experiments [97]. The value of decrease time for millimeter particles (10 mks) is sufficiently greater than experimental one. However, it is necessary to take into consideration that the mixing is not the only process leading to the decrease in conductivity. For example, in pure TNT $\tau \approx 1.9$ mks. One can believe, that the conductivity decrease is mainly due to the diffusive mixing for fine-

disperse compositions, whereas hydrodynamic instabilities play the main role for compositions with medium grain size, and expansion of DP makes the major contribution for the coarse-grained ones. Taking into account this remark, we can claim the satisfactory explanation of the experimental data.

Summary

The simulation results of the interaction between detonation products of heterogeneous HEs show the essential role of hydrodynamic instabilities. The computation results agree in general with known isotope date [98], and with the measurements of the electric conductivity [97]. For the micron size of heterogeneity, the diffusion mixing over sub-microsecond intervals is substantial. For the millimeter grain size, the mixing is low, and for regular RDX size of $\approx$ 200 mkm, the extent of the mixing due to the hydrodynamic interaction during some microseconds can be estimated as substantial.